

Contents lists available at ScienceDirect

Physica D

journal homepage: www.elsevier.com/locate/physd





The instabilities beyond modulational type in a repulsive Bose–Einstein condensate with a periodic potential

Wen-Rong Sun a,*, Jin-Hua Li a,*, Lei Liu b,*, P.G. Kevrekidis c,*

- ^a School of Mathematics and Physics, University of Science and Technology Beijing, Beijing 100083, China
- ^b College of Mathematics and Statistics, Chongqing University, Chongqing, 401331, China
- ^c Department of Mathematics & Statistics, University of Massachusetts, Amherst, MA 01003, USA

ARTICLE INFO

Communicated by V.M. Perez-Garcia

Keywords: Modulational instability Bose–Einstein condensates Hill method High-frequency instability Dark localized events

ABSTRACT

The instabilities of the nontrivial phase elliptic solutions in a repulsive Bose–Einstein condensate (BEC) with a periodic potential are investigated. Based on the defocusing nonlinear Schrödinger (NLS) equation with an elliptic function potential, the well-known modulational instability (MI), the more recently identified high-frequency instability, and an unprecedented – to our knowledge – variant of the MI, the so-called isola instability are identified numerically. Upon varying parameters of the solutions, instability transitions occur through suitable bifurcations, such as the Hamiltonian-Hopf one. Specifically, (i) increasing the elliptic modulus k of the solutions, we find that MI switches to the isola instability and the dominant disturbance has twice the elliptic wave's period, corresponding to a Floquet exponent $\mu = \frac{\pi}{2K(k)}$. The isola instability arises from the collision of spectral elements at the origin of the spectral plane. (ii) Upon varying V_0 , the transition between MI and the high-frequency instability occurs. Differently from the MI and isola instability where the collisions of eigenvalues happen at the origin, the high-frequency instability arises from pairwise collisions of nonzero, imaginary elements of the stability spectrum; (iii) In the limit of sinusoidal potential, we show that MI occurs from a collision of eigenvalues with $\mu = \frac{\pi}{2K(k)}$ at the origin; (iv) we also examine the dynamic byproducts of the instability in chaotic fields generated by its manifestation. An interesting observation is that, in addition to MI, the isola instability could also lead to dark localized events in the scalar defocusing NLS equation.

1. Background and motivation

Bose–Einstein condensates (BECs) trapped in periodic potentials, such as the one induced by standing light waves (optical lattices) have attracted considerable attention already since the early studies on the subject (summarized, e.g., in [1–3]) and even to this day; see, e.g., the recent review of [4]. BECs trapped in standing light waves have been applied to investigate such diverse phenomena as phase coherence [5, 6], matter–wave diffraction [7], quantum logic [8,9] and so on [10,11]. Upon an interplay between periodicity and nonlinearity (even when the interatomic interaction is repulsive), some striking effects appear, such as localized structures [12–14] and instabilities [15–18].

More specifically, the study of instabilities has been a topic of wide interest, as illustrated, e.g., in focused reviews on the subject [19]. Indeed, the modulational instability (MI) has been used experimentally, in conjunction with a magnetic tuning of condensate interactions (from repulsive to attractive) as a method for producing bright solitonic trains and observing their interactions since over 20 years [20]. The

relevant technique has continued to be at the forefront of experimental developments for a considerable while with experimental progress revealing more clearly the nature of solitonic interactions more recently [21]. Indeed, more recent studies have enabled a systematic and even quantitative comparison of experimental outcomes against predictions (e.g., of soliton numbers created by MI) of effective 1d theoretical/computational models [22]. Another dimension of the ever expanding influence and impact the MI more recently has been its experimental use (in conjunction again with a quench from repulsive to attractive interactions) in order to produce – this time in a quasi-two-dimensional setting – of wavepackets leading to the famous Townes soliton [23].

On the discrete (or quasi-discrete) realm of focal interest to this work, the modulational instability has been central to theoretical and experimental implementations not only in atomic BECs, but also in other proximal areas of dispersive wave phenomena. In particular, in BECs in the context of optical lattices the discrete modulational insta-

E-mail addresses: sunwenrong@ustb.edu.cn (W.-R. Sun), m202210704@xs.ustb.edu.cn (J.-H. Li), liueli@126.com (L. Liu), kevrekid@umass.edu

^{*} Corresponding author.

bility was theoretically proposed [24] and subsequently experimentally illustrated [25] to be responsible for a dynamical superfluid-insulator transition for an array of weakly coupled condensates driven by an external harmonic field. Shortly thereafter, such an instability was reported for the first time in the context of nonlinear optics, using an AlGaAs waveguide array with a self-focusing Kerr nonlinearity [26]. Finally, relevant features have been leveraged as a means of producing robust nonlinear coherent structures via MI in other proximal fields featuring discrete media, such as, for instance, in the case of a diatomic granular crystal in the work of [27].

In this paper, we revisit the quasi-discrete setting quasi-onedimensional repulsive BEC trapped in a periodic potential; see, e.g., [13-18,28,29] for only some among numerous examples. Our emphasis is on the study of instabilities and localized structures numerically, utilizing a numerical set of tools that have been developed more recently than some of these important works and which, we believe, reveal a number of unprecedented features and instabilities in the relevant system, worthwhile of further - and potentially also experimental, given the recent developments discussed above - consideration. It is important to appreciate here that at the time of the original works on the system considered herein, the methodological approach leveraged here had not been implemented, to our knowledge, for such problems, and hence the stability analysis of the early works was solely based on dynamical simulations. The latter can easily be inconclusive (e.g., consider an instability with a very small growth rate that may not be manifest over the time horizon of a simulation), and also do not necessarily provide information on the nature of the instability, its predominant length and time scales/growth rates etc. In that vein, the present work, in addition to mathematically establishing a systematic framework for stability, also uncovers unprecedented (to our knowledge, for such systems) instabilities therein which may dominate/supersede the more standardly known modulational instability. Relevant examples are the so-called isola and high-frequency instabilities discussed below. We now proceed to formulate the problem mathematically and discuss some of the main findings.

2. Mathematical formulation and main results

The governing equation is given by the defocusing NLS model with external potential [16,17,28,29]

$$i\psi_t = -\frac{1}{2}\psi_{xx} + |\psi|^2\psi + V(x)\psi,$$
 (1)

where $\psi(x,t)$ is the macroscopic wave function of the condensate. Confinement in a standing light wave leads to V(x) being periodic [15–18],

$$V(x) = -V_0 \text{sn}^2(x, k), \tag{2}$$

where $\operatorname{sn}^2(x,k)$ is the Jacobian elliptic sine function with elliptic modulus $k \in [0,1]$. When k=0, $\operatorname{sn}(x,k)$ becomes $\operatorname{sin}(x)$ and the potential V(x) is a standing light wave [3]. As discussed in [14,17], when k<0.9, the potential V(x) resembles the behavior of $\operatorname{sin}(x)$ and the latter could provide a good approximation to a standing light wave, while at the same time retaining the advantage of analytically tractable solutions that were leveraged toward a number of analytical results in the above works.

Following [16,17], there have been many works based on the NLS-type equations with periodic potentials in the context of BECs. Stability of the trivial phase solutions of the defocusing NLS with periodic potential in two dimensions was studied in [30]. The stability properties of the trivial phase solutions in two-component BECs trapped in an external elliptic function potential were investigated in [14]. A proof of the existence of dark solitons in a NLS equation with a periodic potential was given in [31]. The authors in [32] produced exact periodic and soliton solutions to the Gross–Pitaevskii equation with the pseudopotential in the form of a nonlinear lattice, induced by a spatially periodic modulation of the local nonlinearity. Stationary

solutions for the NLS equation modeling repulsive BEC in a small potential were obtained through a form of nonlinear perturbation [33]. Very recently, the authors in [34] investigated theoretically and experimentally the quenching of the superfluid density of a dilute BEC due to the breaking of translational invariance by an external 1D periodic potential. In 2023, the authors in [35] studied the instabilities of a BEC in periodic potentials and they used an out-of-phase linear lattice to stabilize the lowest-energy Bloch states of BECs. Importantly, these very recent works suggest a renewal of interest in theoretical, computational, but also notably experimental consideration of optical lattice settings, accompanied by the much more substantial tunability and controllability thereof presently available [34]. Besides, the authors in [36] demonstrated that the interplay between a nonlinearity and PT symmetry in a periodic potential results in peculiar features of nonlinear periodic solutions. We also refer to [37-39] (recent publications) for the dynamics of BECs in periodic potentials.

The stationary condensates are described by the solutions to (1) of the form [16,17]:

$$\psi(x,t) = r(x)\exp(-i\omega t + i\theta(x)),\tag{3}$$

where $\theta(x)=c\int_0^x \frac{dx'}{r^2(x')}$ and $r^2(x)=A \operatorname{sn}^2(x,k)+B$. Besides, the relations among the parameters ω , c, A, B, V_0 and k are $\omega=\frac{1}{2}\left(1+k^2+3B-\frac{BV_0}{V_0+k^2}\right)$, $c^2=B\left(1+\frac{B}{V_0+k^2}\right)\left(V_0+k^2+Bk^2\right)$ and $A=V_0+k^2$. To require that $r^2(x)>0$ and $c^2>0$ implies the following conditions: $V_0\geq -k^2$ and $V_0\leq -k^$

(i) It is well known that the modulational instability (MI), also known – especially so in the context of fluids – as the Benjamin–Feir instability, originated from the study of stability of Stokes waves in deep water (in the late 1960s) [40]. Subsequently, MI has been predicted and observed in BECs [20-22,24,25,41-45] and nonlinear optics [46-51], as well as in other physical media [52-54]. In 2011, Deconinck and Oliveras [55] first displayed the full stability spectra of Stokes waves in finite and infinite depth. More importantly, they showed that in addition to MI, other instabilities, taking place away from the origin of the so-called spectral plane (the plane of the imaginary vs. the real part of the corresponding eigenvalues) exist. The instabilities are also referred to as high-frequency instabilities. These high-frequency instabilities have been studied analytically [56,57]. Therefore, a natural question arises: Do these high-frequency instabilities (originating in the fluid setting) exist in BECs? In this paper, we show the existence of the high-frequency instability in BECs and study the transition between the high-frequency instability and MI in the context of the model of Eq. (1) with the potential of Eq. (2).

Additionally, in 2022, the authors of [58] studied the instability of near-extreme Stokes waves. One important feature identified in [58] is the appearance of what we refer to as the isola instability branch. For such an instability, the eigenvalues in the case of [58] correspond to eigenfunctions that are localized near the wave crest as the extreme wave is approached. Importantly, a telltale sign of such an instability that we will use to distinguish it from MI is that it detaches from the origin of the spectral plane and corresponds to a band of complex eigenvalues that thereafter remains detached from the origin (contrary to the case of MI, where the band encompasses the origin). The transition between isola instability and MI is investigated. We expect that such an instability branch may be tractable in BECs, based on the above significant and quantitative experimental progress therein [21–23].

(ii) The standard defocusing NLS equation (i.e., $V_0=0$ in (1)) does not admit localized solutions on the unstable backgrounds (such as rogue-wave solutions) since all periodic traveling solutions (including

plane-wave solutions) of the defocusing NLS equation are stable. However, by considering the external potential in the defocusing regime, i.e., $V_0 \neq 0$ in (1), we show that different instabilities occur. Therefore, a natural question arises: do some localization events exist in the defocusing NLS equation with an elliptic function potential? It is well known that MI could lead to the formation of localization events [59–63]. In particular, it is especially interesting (given its recent identification) to explore whether specifically the *isola instability* could lead to localized events. Indeed, the present work illustrates the dynamical evolutions that showcase how this phenomenon takes place.

3. Computational technique of choice: Hill's method and its setup

The linear stability of (3) in the setting of the model of Eq. (1) is explored by considering the following form:

$$\psi(x,t) = (r(x) + \epsilon \phi(x,t)) \exp[i(\theta(x) - \omega t)], \tag{4}$$

where $\epsilon \ll 1$ denotes a small parameter. With $\mathbf{U} = (U_1, U_2)^T = (\text{Re}[\phi], \text{Im}[\phi])^T = \hat{\mathbf{U}}(x) \exp(\lambda t) + c.c. = (\hat{U}_1, \hat{U}_2)^T \exp(\lambda t) + c.c.$, the eigenvalue problem is expressed as [16,17],

$$\mathcal{L}\hat{\mathbf{U}} = \begin{pmatrix} -\frac{c}{r(x)} \partial_x \frac{1}{r(x)} & L_- \\ -L_+ & -\frac{c}{r(x)} \partial_x \frac{1}{r(x)} \end{pmatrix} \hat{\mathbf{U}} = \lambda \hat{\mathbf{U}}, \tag{5}$$

where

$$L_{+} = -\frac{1}{2} \left(\partial_{x}^{2} - \frac{c^{2}}{r^{4}(x)} \right) + 3r^{2}(x) + V(x) - \omega, \tag{6}$$

$$L_{-} = -\frac{1}{2} \left(\partial_{x}^{2} - \frac{c^{2}}{r^{4}(x)} \right) + r^{2}(x) + V(x) - \omega, \tag{7}$$

and λ is a complex number, i.e., the corresponding eigenvalue of the linearization. The growth rate γ is defined as the real part of λ (if positive). Here, +c.c. denotes that the complex conjugate of the previous term is added. We note that when c=0, the stability problem (5) corresponds to the trivial phase solutions. This case was examined in [16,17]. We only focus on the stability problem of the nontrivial phase solutions ($c \neq 0$) using the so-called Hill's method that was originally theoretically developed and computationally implemented in [64].

Since the coefficient functions of the stability problem (5) are periodic in x with period L=2K(k), we write all coefficient functions as the complex Fourier form, i.e., $r^2(x)=\sum_{n=-\infty}^\infty Q_n e^{i2n\pi x/L}$, $r^{-2}(x)=\sum_{n=-\infty}^\infty R_n e^{i2n\pi x/L}$, $r^{-4}(x)=\sum_{n=-\infty}^\infty S_n e^{i2n\pi x/L}$, $r^{-3}(x)r'(x)=\sum_{n=-\infty}^\infty T_n e^{i2n\pi x/L}$, and $V(x)=\sum_{n=-\infty}^\infty \hat{V}_n e^{i2n\pi x/L}$. Here Q_n , R_n , S_n , T_n and \hat{V}_n denote the Fourier coefficients. The periodicity of coefficient functions of (5) allows us to decompose the perturbations using Floquet's Theorem (see [64] for details)

$$\hat{U}_1(x) = e^{i\mu x} H_1(x) = e^{i\mu x} \sum_{n = -\infty}^{\infty} \hat{U}_{1n} e^{i2n\pi x/PL},$$
(8)

$$\hat{U}_2(x) = e^{i\mu x} H_2(x) = e^{i\mu x} \sum_{n = -\infty}^{\infty} \hat{U}_{2n} e^{i2n\pi x/PL},$$
(9)

where the Floquet exponent $\mu \in [0, 2\pi/L)$, and

$$\hat{U}_{1n} = \frac{1}{PL} \int_{-PL/2}^{PL/2} H_1(x) e^{-i2\pi nx/PL} dx,$$
(10)

$$\hat{U}_{2n} = \frac{1}{PL} \int_{-PL/2}^{PL/2} H_2(x) e^{-i2\pi nx/PL} dx.$$
 (11)

Here, we expand $H_1(x)$ and $H_2(x)$ as a Fourier series in x with period PL, where $P \in \mathbb{N}$. Substituting all of the above Fourier expansions into (5) and equating Fourier coefficients lead to the following bi-infinite eigenvalue problem:

$$-\left(\omega - \frac{1}{2}\left(i\mu + \frac{i2n\pi}{PL}\right)^{2}\right)\hat{U}_{2n} + \sum_{m=-\infty}^{\infty} Q_{\frac{n-m}{P}}\hat{U}_{2m} + \sum_{m=-\infty}^{\infty} \hat{V}_{\frac{n-m}{P}}\hat{U}_{2m} + \frac{c^{2}}{2}\sum_{m=-\infty}^{\infty} S_{\frac{n-m}{P}}\hat{U}_{2m}$$
(12a)

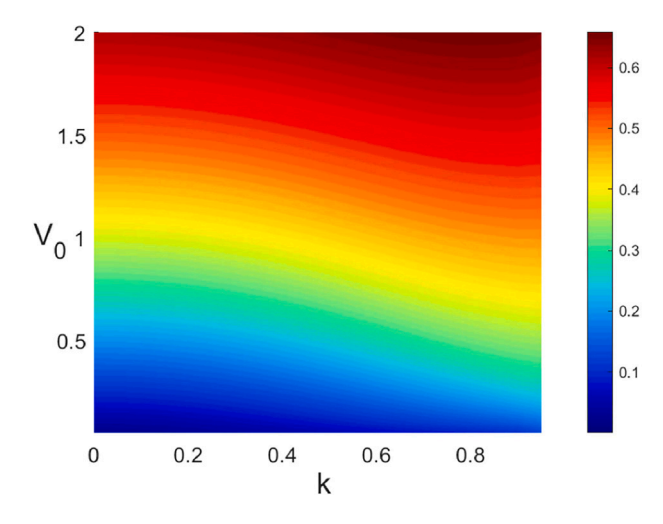


Fig. 1. The maximal instability growth rate γ as a function of k and V_0 with B=0.25.

$$+ c \sum_{m=-\infty}^{\infty} T_{\frac{n-m}{P}} \hat{U}_{1m} - c \sum_{m=-\infty}^{\infty} R_{\frac{n-m}{P}} \hat{U}_{1m} = \lambda \hat{U}_{1n},$$

$$\left(\omega - \frac{1}{2} \left(i\mu + \frac{i2n\pi}{PL}\right)^{2}\right) \hat{U}_{1n} - 3 \sum_{m=-\infty}^{\infty} Q_{\frac{n-m}{P}} \hat{U}_{1m}$$

$$- \sum_{m=-\infty}^{\infty} \hat{V}_{\frac{n-m}{P}} \hat{U}_{1m} - \frac{c^{2}}{2} \sum_{m=-\infty}^{\infty} S_{\frac{n-m}{P}} \hat{U}_{1m}$$

$$+ c \sum_{m=-\infty}^{\infty} T_{\frac{n-m}{P}} \hat{U}_{2m} - c \sum_{m=-\infty}^{\infty} R_{\frac{n-m}{P}} \hat{U}_{2m} = \lambda \hat{U}_{2n},$$
(12b)

where $Q_{\frac{n-m}{P}}, R_{\frac{n-m}{P}}, S_{\frac{n-m}{P}}, T_{\frac{n-m}{P}}, \hat{V}_{\frac{n-m}{P}} = 0$ if n-m is not divisible by P. The bi-infinite eigenvalue problem (12) is equivalent to (5). We will determine the spectrum of the linearized operator about the stationary solutions using the bi-infinite eigenvalue problem (12). The whole stability spectrum of the elliptic solutions is constructed as the union of the spectra for all values of μ in $\left[0,\frac{2\pi}{L}\right)$. Specifically, we consider the whole stability spectrum in the λ plane by choosing 9999 different

Floquet exponents in $\mu \in \left[0, \frac{2\pi}{L}\right)$ and 41 Fourier modes, so as to ensure that we appropriately resolve the relevant spectral bands.

4. Instability results

In this section, by choosing a cut-off N on the number of Fourier modes, we numerically find the spectrum to (5) using the bi-infinite eigenvalue problem (12).

4.1. From MI to isola instability

Note that the solutions (3) have three free parameters V_0 , B and k. Fig. 1 shows the maximal instability growth rate γ as a function of k and V_0 with B = 0.25. We can see that γ increases with k and V_0 increasing. To study the transition from MI to isola instability, by fixing $V_0 = 1$ and B = 0.25, we study the dynamics of instabilities with varying k, i.e., effectively varying the periodicity of the potential. As shown in Fig. 2, for $0 < k < k_c = 0.63936$, the only instability of the elliptic wave is the MI and the maximal instability growth rate γ corresponds to the real eigenvalues with $\mu = \frac{\pi}{2K(k)}$, which implies that the dominant disturbance has twice the period of elliptic wave. A typical example of MI is shown in Fig. 2(a) with $k = 0.55 \in (0, k_c)$ and it can be seen that the closure of spectrum that is not on the imaginary axis forms an infinity symbol centered at the spectral plane origin. At $k = k_c$, the collisions of eigenvalues on the imaginary axis (at $\pm 0.06202i$), lead to the appearance of an ellipse-like curve. Then from k_c to $k_e = 0.64921$, two types of instability appear, as shown in Fig. 2(d) with k = 0.64,

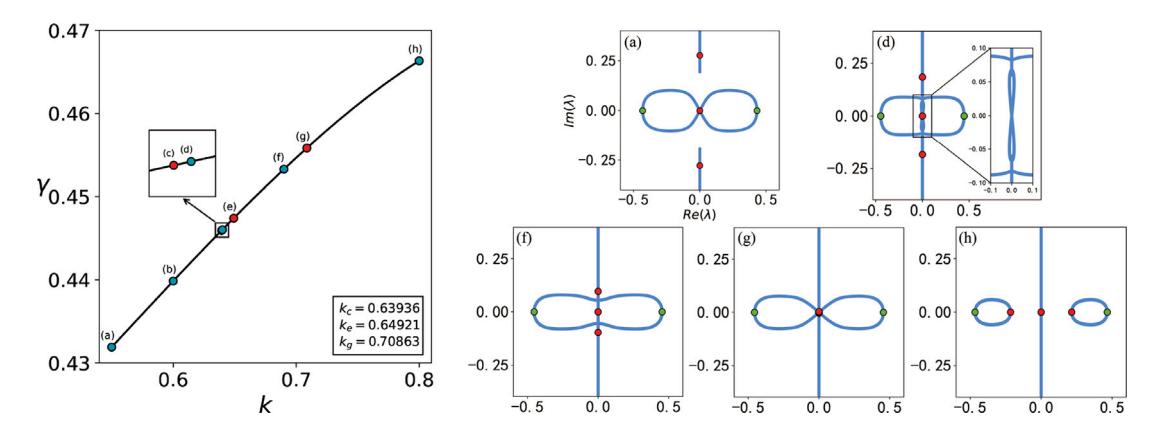
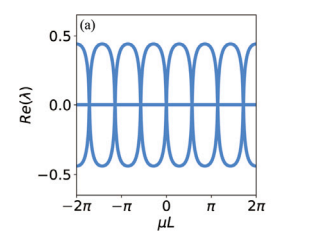


Fig. 2. Left panel shows the maximal instability growth rate γ as a function of k with B=0.25 and $V_0=1$. When $k < k_c$, the modulation instability appears [one example can be seen in (a) (with k=0.55) of the right panel]. At $k=k_c$, the ellipse-like curve appears. From k_c to k_e , the dominant instability switches to the ellipse-like instability [one example can be seen in (d) (with k=0.64) of the right panel]. At $k=k_e$, MI disappears and only the ellipse-like eigenvalues exist. From k_e to k_g , the ellipse-like curve is compressed vertically [as shown in (f) (with k=0.69) of the right panel]. An infinity symbol forms at k_g (as shown in (g) of the right panel). When $k>k_g$, the infinity symbol splits into two isolas drifting away along the real axis [as shown in (h) (with k=0.8) of the right panel]. For the right panel, the red dots correspond to $\mu=0$ and the green dots correspond to $\mu=0$ and $\mu=0$ are $\mu=0$ and $\mu=0$ and $\mu=0$ are $\mu=0$ and $\mu=0$ are $\mu=0$ and $\mu=0$ are $\mu=0$ and



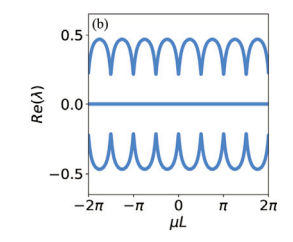
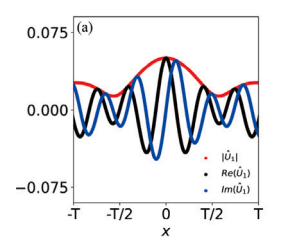


Fig. 3. Real part of growth rates as a function of the Floquet parameter μ . Here the parameters of (a) (MI with k=0.6) are the same as point (b) in the left panel of Fig. 2 and the parameters of (b) (isola instability with k=0.8) are the same as point (h) in the left panel of Fig. 2.



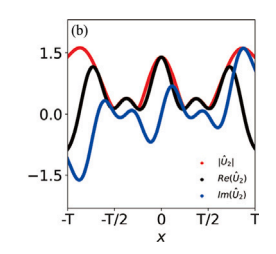


Fig. 4. Eigenfunctions of the isola instability branch for $\mu = \frac{x}{2K(k)}$ and the parameters are the same as point (h) in the left panel of Fig. 2. Here (a) and (b) correspond to the cases of \hat{U}_1 and \hat{U}_2 , respectively.

which shows that a Figure 8 pattern is present inside an ellipse-like curve. Therefore from k_c to k_e , the dominant instability switches to the ellipse-like instability, which is different from MI (recall that MI involves an unstable band of eigenvalues encompassing the origin), and the dominant disturbance has twice period of elliptic waves. At $k=k_e$, a collision of eigenvalues at the origin leads to the disappearance of MI and only the ellipse-like eigenvalues exist. From k_e to $k_g=0.70863$, the ellipse-like curve is compressed vertically (see Fig. 2(f) with k=0.69). Finally, this leads to the formation of an infinity symbol at $k_g=0.70863$ (see Fig. 2(g)), again of the MI type.

Increasing $k>k_g$, the collision of the eigenvalues with $\mu=0$ (red dots in Fig. 2 (f,g,h)) at the origin (where a Hamiltonian–Hopf bifurcation occurs) causes the infinity symbol to subsequently split into two isolas drifting away along the real axis, as shown in Fig. 2(h) with k=0.8. Now, the dominant instability switches to the isola instability, which is not MI (since the latter involves the spectral plane origin), and the dominant disturbance retains twice the period of the elliptic wave.

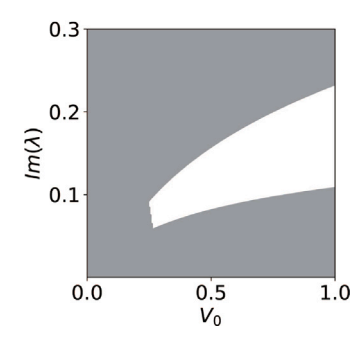


Fig. 5. Imaginary part of λ as a function of V_0 with B = 0.25 and k = 0.5. The non-zero imaginary parts of the eigenvalues form the gray region, while the white region indicates the (potential, for suitable values of V_0) frequency gap.

For the isola instability, we can observe the following. (a) Similarly to MI, the entire range of the Floquet parameter μ covers the isola instability branch (as shown in Fig. 3), in contrast to the high-frequency instabilities corresponding to a narrow region of the Floquet parameter μ (as shown in Fig. 7 below); (b) differently from the MI, the spectrum of the isola instability has no intersections with the origin and the range of growth rate does not start from zero but from the nonzero eigenvalues with $\mu = 0$, as shown in Fig. 3; (c) The maximal instability growth rate corresponds to the real eigenvalues with $\mu = \frac{\pi}{2K(k)}$ (as shown in the green dots of Fig. 2(h)); (d) such an isola instability branch is called local instability branch in fluids [58], since the eigenfunctions associated with such a branch change rapidly in the vicinity of the wave-crest. However, here the eigenfunctions associated with such a branch do not have such local property (which is a fundamental difference in comparison to [58]), as shown in Fig. 4. Therefore, such isola instability in BECs can be deemed to be nontrivially distinct from the local instability branch in fluids. Besides, we show a band gap structure by studying the relation between the imaginary part of λ and V_0 , as shown in Fig. 5. In fact, for every V_0 , we obtain a set of eigenvalues. The non-zero imaginary parts of these eigenvalues form the gray region. This illustrates how, at a finite positive value of V_0 , a frequency gap emerges, subsequently growing as a function of V_0 .

4.2. From MI to high-frequency instability

To study the transition from MI to high-frequency instability, by fixing k=0.5 and B=0.3, we study the dynamics of instabilities

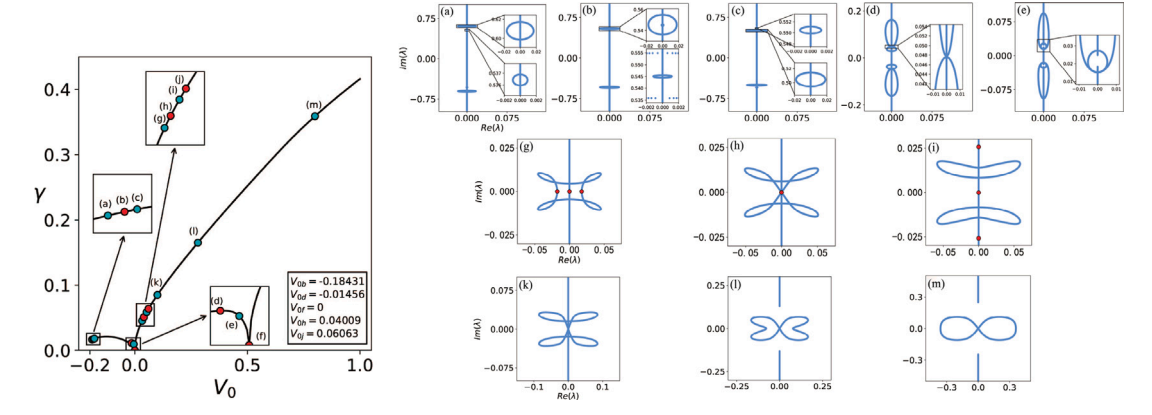


Fig. 6. (Left panel) The maximal instability growth rate γ as a function of V_0 . When $V_0 = V_{0f}$, the elliptic solutions are stable. When $-0.19 < V_0 < V_{0b} = -0.18431$, the first bubble dominates the instability (see (a) (with $V_0 = -0.19$) of the right panel). From V_0 to V_{0b} , the two bubbles approach and collide (see (b) of the right panel). When $V_0 > V_{0b}$, the two bubbles pass through each other (see (c) (with $V_0 = -0.18$) of the right panel) and then they fuse together (see (d) (with $V_0 = -0.01456$) of the right panel) and move toward the origin (see (e) (with $V_0 = -0.005$) of the right panel). When $0 < V_0 < V_{0f} = 0.06063$, a transition between different stability spectra caused by the collision of eigenvalues with $\mu = 0$ at the origin happens (see (g, h, i)) (with $V_0 = 0.032, 0.04009, 0.052$) of the right panel). The red dots in (g, h, i) of the right panel correspond to $\mu = 0$. When $V_0 > V_{0f}$, we show three different stability spectra (see (k, l, m)) (with $V_0 = 0.1, 0.28, 0.89$) of the right panel).

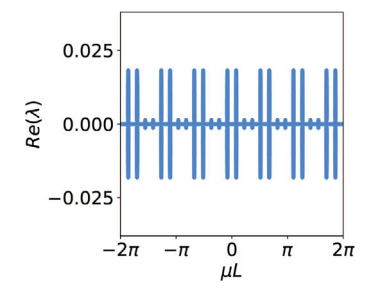


Fig. 7. Real part of growth rates as a function of the Floquet parameter μ . The parameters are the same as point (c) in the left panel of Fig. 6.

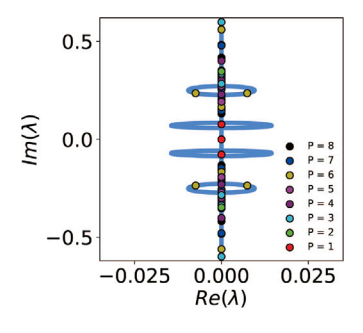


Fig. 8. The stability spectrum for the elliptic solutions (3) with respect to *P*-subharmonic perturbations (k = 0.5, B = 0.3 and $V_0 = -0.04$).

with varying V_0 . We note that when $V_0=V_{0f}=0$, (1), the problem reduces to the standard defocusing NLS equations with well known that all elliptic solutions with $V_0=0$ are stable [65]. Here we consider the case where $V_0\neq 0$. As shown in Fig. 6, when $V_0<0$, only the high-frequency instability occurs (see Fig. 6(a,b,c,e)). The high-frequency instability (the corresponding perturbations oscillate in time) develops from a Hamiltonian–Hopf bifurcation: collisions of nonzero, imaginary elements of the stability spectrum ($V_0=0$) lead to eigenvalues symmetrically bifurcating from the imaginary axis as V_0 decreasing, resulting in instability. Specifically, from $-0.19 \leqslant V_0 < V_{0b} = -0.18431$, the first bubble (arising farther away from the origin) dominates the instability (see Fig. 6(a) with $V_0=-0.19$). By increasing V_0 to V_{0b} , the two bubbles approach and collide (see Fig. 6(b)). When $V_0>V_{0b}$, the two bubbles pass through each other (see Fig. 6(c) with $V_0=-0.185$) and subsequently they fuse together (see Fig. 6(d) with $V_0=-0.01456$) and

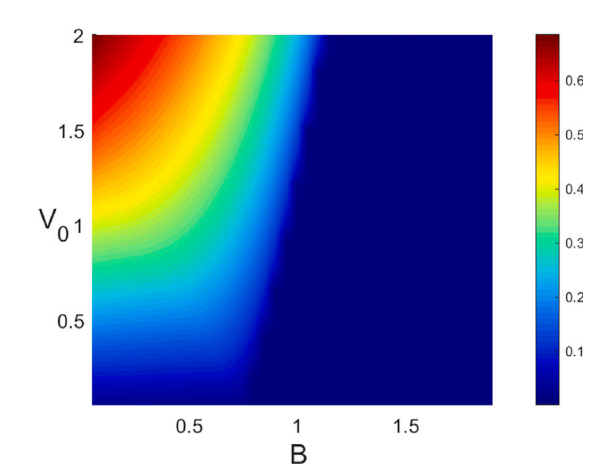


Fig. 9. The maximal instability growth rate γ as a function of B and V_0 with k=0.

move toward the origin (see Fig. 6(e) with $V_0=-0.005$). When $0 < V_0 < V_{0j}=0.06063$, the elliptic solutions are modulational stable. We can see the transition between different stability spectra caused by the collision of eigenvalues with $\mu=0$ at the origin (see Fig. 6(g,h,i)). When $V_0>V_{0j}$, the modulation instability appears and we show three different stability spectra (see Fig. 6(k,l,m)). Differently from MI and the isola instability, we can see that the high-frequency instability branch occurs in a narrow region of the Floquet parameter μ (as shown in Fig. 7), which implies that we may get some useful stability results with respect to subharmonic perturbations. For example, we show that the elliptic solutions (3) (with k=0.5, B=0.3 and $V_0=-0.04$) are stable with respect to 1-, 2-, 3-, 4- , 5-, 7- and 8- subharmonic perturbations but unstable with respect to the 6- subharmonic perturbation, as shown Fig. 8.

4.3. Instability trapped in a standing light wave (k = 0)

When k=0, the elliptic potential V(x) reduces to the trigonometric functions and thus V(x) is a standing light wave. Fig. 9 shows the maximal instability growth rate γ as a function of B and V_0 with k=0. We can see that γ increases with V_0 increasing and B decreasing. The MI arises from the collision of the eigenvalues with $\mu=\frac{\pi}{2K(k)}$ at the origin, as shown in Fig. 10. Here, we also note that in Fig. 10 a panel with four petals morphs into a panel with two petals. This is because

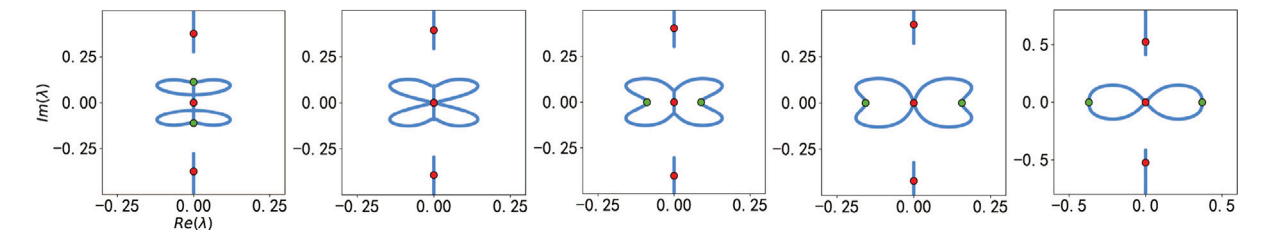


Fig. 10. The stability spectrum for the elliptic solutions (3) with k = 0, B = 0.29, (from left to right) $V_0 = 0.3$, $V_0 = 0.36166$, $V_0 = 0.4$, $V_0 = 0.48$ and $V_0 = 1$.

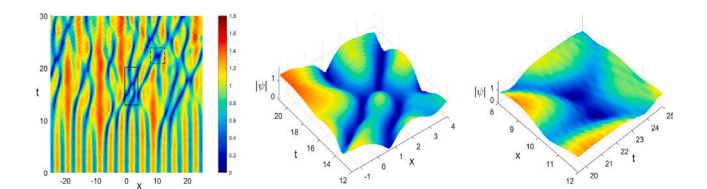


Fig. 11. Numerical evolution of the MI resulting in pattern distortion and collisional events (highlighted by boxes on the left panel and zoomed-in at the middle and right panels). The initial condition is solution (3) perturbed by 5% random noise with k=0.6, B=0.25 and $V_0=1$. The amplitude evolution (upper-left); the (solid-line) zoomed-in evolution of the box on the upper-left is shown on the middle panel; the (dotted-line) zoomed-in evolution of the box on the left is shown on the rightmost panel.

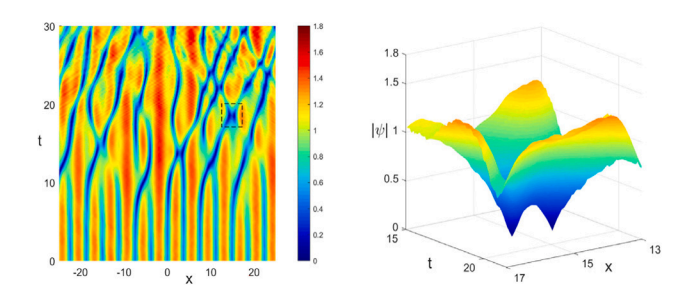


Fig. 12. Numerical excitation of the isola instability. The initial condition is solution (3) perturbed by 5% random noise with k=0.72, B=0.25 and $V_0=1$. The amplitude evolution (left); the zoomed-in evolution of the box on the left is shown on the right panel.

increasing V_0 leads to more collisions of imaginary eigenvalues at the origin and the spectral curve is vertically compressed. Besides we note that solutions (3) with k=0 and b=0.29 are stable with respect to co-periodic perturbations. When V_0 is large enough, it can be seen that the maximal instability growth rate corresponds to the real eigenvalues with $\mu=\frac{\pi}{2K(k)}$, as shown in Fig. 10 with $V_0=1$.

4.4. Dynamical manifestation of the instabilities

Having explored the different scenarios of instability, we now turn to direct numerical simulations in order to explore the dynamical byproducts of these instabilities. Starting from the nontrivial phase elliptic solutions (3), we impose random perturbations and visualize the patterns produced by (1) numerically.

The case of dynamical evolution of a modulationally unstable scenario is shown in Fig. 11. One can observe that after an initial stage, the periodic pattern is distorted leading to the emergence of some skewed density dips reminiscent of moving dark (gray) solitary waves; for details of such coherent structures, see the review of [66]. As these structures move through the distorted pattern they appear to interact in collision-type events which are somewhat reminiscent of the interactions of dark solitary waves observed, e.g., in the experiments of [67–69]. These types of events causing a (deeper) spatio-temporal dip, prior to the colliding patterns re-emerging are highlighted in two

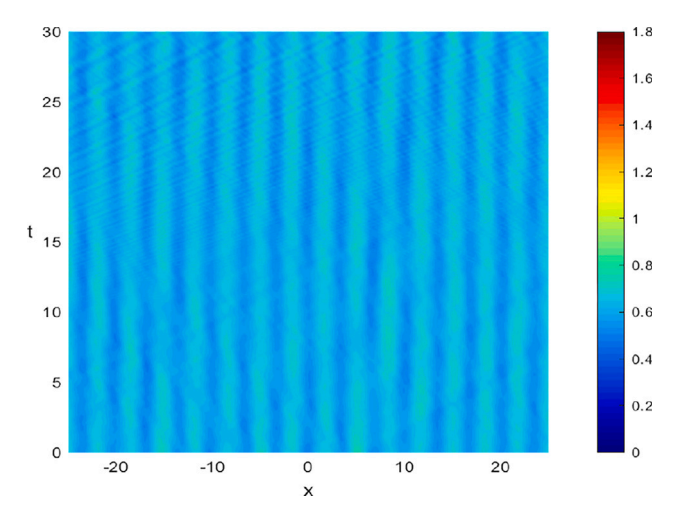


Fig. 13. Here, the initial condition is solution (3) perturbed by 5% random noise with k = 0.5, B = 0.3 and $V_0 = -0.1$.

boxes in Fig. 11 whose evolution is presented in more detail in the additional panels of the figure.

Interestingly, and as perhaps may be expected by the similar nature of the relevant instability (although the isola instability is detached from the spectral plane origin), the dynamics of the isola instability is similar to that of MI. Indeed, the relevant dynamical manifestations can be seen in Fig. 12. Here, too, it is evident that the distortion of the pattern leads to a number of waves that propagate along skewed lines in the space–time (left) panel of the figure. The zoom-in to the box of the left panel is once again shown in the right panel, illustrating a space–time collisional type event before the participating waves once again separate. It is relevant to note here that similar results to those of Figs. 11-12 arise in the case of k=0, i.e., for a trigonometric standing wave of light (results not shown here).

Finally, it is interesting to point out the fundamental difference of the high-frequency instability, in comparison, e.g., with those of Figs. 11–12 above. A prototypical example of the high-frequency instability is shown in Fig. 13. We can see that the instability is manifested through the propagation of high-wavenumber unstable modes which, in turn, are weakly perturbing the (deeper) density dips of the original configuration. Nevertheless, the latter persist, avoiding the more intense collisional events described above.

5. Conclusions & future challenges

The instabilities of the nontrivial phase elliptic solutions in a repulsive Bose–Einstein condensate (BEC) with a periodic potential have been studied. Based on the defocusing nonlinear Schrödinger (NLS) equation with an elliptic function potential and on a sequence of fundamental earlier works [15–18], the MI, the similar to it isola instability (on the real line) and the rather different high-frequency instability have been observed numerically and have been elucidated

quantitatively. With varying parameters in solutions and equation, instability transitions occur, e.g., through a Hamiltonian-Hopf bifurcation. Specifically, (i) increasing k, we have observed that the MI switches to the isola instability and the dominant disturbances have twice the elliptic wave's period, corresponding to a Floquet exponent $\mu = \frac{\pi}{2K(k)}$. The isola instability arises from the collision of spectral elements at the origin with $\mu = 0$; (ii) with varying V_0 , the transition between the MI and high-frequency instability occurs. Different from the MI and isola instability where the collisions of spectral elements happen at the origin, the high-frequency instability arises from pairwise collisions of nonzero, imaginary elements of the stability spectrum; (iii) in the limit of sinusoidal potential, with varying V_0 , we have shown the MI occurs from a collision of eigenvalues with $\mu = \frac{\pi}{2K(k)}$ at the origin; (iv) the dynamical evolution of the relevant instabilities has been elucidated, notably leading in the case of the MI and isola instabilities to the distortion of the patterns and events resembling the collision of dark (gray) solitary waves.

Admittedly, since the emergence of these fundamental works [15–18], numerous developments have arisen in higher-dimensional BECs [70], in multi-component condensates [71,72], as well as in the context of long-range interactions [73]. Extending the present considerations to these progressively more and more accessible settings would be a natural next step for future studies.

CRediT authorship contribution statement

Wen-Rong Sun: Conceptualization, Formal analysis, Investigation, Methodology, Software, Supervision, Validation, Visualization, Writing – original draft, Writing – review & editing. Jin-Hua Li: Software, Writing – review & editing. P.G. Kevrekidis: Conceptualization, Investigation, Methodology, Supervision, Validation, Visualization, Writing – original draft, Writing – review & editing.

Declaration of competing interest

The authors declare that they have no known competing financial interests or personal relationships that could have appeared to influence the work reported in this paper.

Data availability

No data was used for the research described in the article.

Acknowledgments

This work has been supported by the Fundamental Research Funds of the Central Universities (No. 230201606500048) and the National Natural Science Foundation of China under Grant No. 12205029. The work of P.G.K is supported by the US National Science Foundation under Grants No. PHY-2110030 and DMS-2204702).

References

- C.J. Pethick, H. Smith, Bose–Einstein Condensation in Dilute Gases, Cambridge University Press, Cambridge, 2008.
- [2] L.P. Pitaevskii, S. Stringari, Bose–Einstein Condensation and Superfluidity, Oxford University Press, Oxford, 2016.
- [3] O. Morsch, M. Oberthaler, Rev. Modern Phys. 78 (2006) 179.
- [4] E. Kengne, W.M. Liu, B.A. Malomed, Phy. Rep. 899 (2021) 1.
- [5] B.P. Anderson, M.A. Kasevich, Science 282 (1998) 1686.
- [6] E.W. Hagley, L. Deng, M. Kozuma, J. Wen, K. Helmerson, S.L. Rolston, W.D. Phillips, Science 283 (1999) 1706.
- [7] Y.B. Ovchinnikov, J.H. Muller, M.R. Doery, E.J.D. Vredenbregt, K. Helmerson, S.L. Rolston, W.D. Phillips, Phys. Rev. Lett. 83 (1999) 284.
- [8] D. Jaksch, C. Bruder, J.I. Cirac, C.W. Gardiner, P. Zoller, Phys. Rev. Lett. 81 (1998) 3108.

- [9] G.K. Brennen, C.M. Caves, P.S. Jessen, I.H. Deutsch, Phys. Rev. Lett. 82 (1999) 1060
- [10] D.I. Choi, O. Niu, Phys. Rev. Lett. 82 (1999) 2022.
- [11] L.D. Carr, J. Brand, Phys. Rev. A 70 (2004) 033607.
- [12] Y.S. Kivshar, G.P. Agrawal, Optical Solitons: From Fibers to Photonic Crystals, Academic, New York, 2003.
- [13] T.J. Alexander, E.A. Ostrovskaya, Y.S. Kivshar, Phys. Rev. Lett. 96 (2006) 040401.
- [14] N.A. Kostov, V.Z. Enol'skii, V.S. Gerdjikov, V.V. Konotop, M. Salerno, Phys. Rev. E 70 (2004) 056617.
- [15] J.C. Bronski, L.D. Carr, R.C. González, B. Deconinck, J.N. Kutz, K. Promislow, Phys. Rev. E 64 (2001) 056615.
- [16] J.C. Bronski, L.D. Carr, B. Deconinck, J.N. Kutz, Phys. Rev. E 63 (2001) 036612.
- [17] J.C. Bronski, L.D. Carr, B. Deconinck, J.N. Kutz, Phy. Rev. Lett. 86 (2001) 1402.
- [18] J.C. Bronski, Z. Rapti, Dynam. Partial Differ. Equ. 2 (2005) 335.
- [19] P.G. Kevrekidis, D.J. Frantzeskakis, Modern Phys. Lett. B 18 (2004) 173.
- [20] K.E. Strecker, G.B. Partridge, A.G. Truscott, R.G. Hulet, Nature 417 (2002) 150.
- [21] J.H.V. Nguen, D. Luo, R.G. Hulet, Science 356 (2017) 422.
- [22] P.J. Everitt, M.A. Sooriyabandara, M. Guasoni, P.B. Wigley, C.H. Wei, G.D. McDonald, K.S. Hardman, P. Manju, J.D. Close, C.C.N. Kuhn, S.S. Szigeti, Y.S. Kivshar, N.P. Robins, Phys. Rev. A 96 (2017) 041601, (R).
- [23] C.A. Chen, C.L. Hung, Phys. Rev. Lett. 125 (2020) 250401.
- [24] A. Smerzi, A. Trombettoni, P.G. Kevrekidis, A.R. Bishop, Phys. Rev. Lett. 89 (2002) 170402.
- [25] F.S. Cataliotti, L. Fallani, F. Ferlaino, C. Fort, P. Maddaloni, M. Inguscio, New J. Phys. 5 (2003) 71.
- [26] J. Meier, G.I. Stegeman, D.N. Christodoulides, Y. Silberberg, R. Morandotti, H. Yang, G. Salamo, M. Sorel, J.S. Aitchison, Phys. Rev. Lett. 92 (2004) 163902.
- [27] N. Boechler, G. Theocharis, S. Job, P.G. Kevrekidis, Mason A. Porter, C. Daraio, Phys. Rev. Lett. 104 (2010) 244302.
- [28] F. Dalfovo, S. Giorgini, L.P. Pitaevskii, S. Stringari, Rev. Modern Phys. 71 (1999) 463
- [29] L.D. Carr, C.W. Clark, W.P. Reinhardt, Phys. Rev. A 62 (2000) 063610.
- [30] B. Deconinck, B.A. Frigyik, J.N. Kutz, Phys. Lett. A 283 (2001) 177.
- [31] P.J. Torres, V.V. Konotop, Comm. Math. Phys. 282 (2008) 1.
- [32] C.H. Tsang, Boris A. Malomed, K.W. Chow, Discrete Cont. Dyn-S 5 (2011) 1299.
- [33] K. Mallory, R.A. Van Gorder, Phys. Rev. E 88 (2013) 013205.
- [34] G. Chauveau, C. Maury, F. Rabec, C. Heintze, G. Brochier, S. Nascimbene, J. Dalibard, J. Beugnon, S.M. Roccuzzo, S. Stringari, Phys. Rev. Lett. 130 (2023) 226003.
- [35] J. Hong, C. Wang, Y. Zhang, Phys. Rev. E 107 (2023) 044219.
- [36] Y. Zhang, Z. Chen, B. Wu, T. Busch, V.V. Konotop, Phys. Rev. Lett. 127 (2021) 034101.
- [37] P. Yang, X. Li, Y. Tian, J. High Energ. Phys. 2021 (2021) 190.
- [38] X. Luo, Z. Hu, Z.Y. Zeng, Y. Luo, B. Yang, J. Xiao, I. Li, A.X. Chen, Phys. Rev. A 103 (2021) 063324.
- [39] J. Bera, A.Q. Batin, S. Ghosh, B. Malomed, U. Roy, Phil. Trans. R. Soc. A. 381 (2023) 2022007.
- [40] T.B. Benjamin, J. Feir, J. Fluid Mech. 27 (1967) 417.
- [41] V.V. Konotop, M. Salerno, Phys. Rev. A 65 (2002) 021602.
- [42] L. Salasnich, A. Parola, L. Reatto, Phys. Rev. Lett. 91 (2003) 080405.
- [43] G. Theocharis, Z. Rapti, P.G. Kevrekidis, D.J. Frantzeskakis, V.V. Konotop, Phys. Rev. A 67 (2003) 063610.
- [44] L.D. Carr, J. Brand, Phys. Rev. Lett. 92 (2004) 040401.
- [45] S. Ro jas Ro jas, R.A. Vicencio, M.I. Molina, F. Kh. Abdullaev, Phys. Rev. A 84 (2011) 033621.
- [46] A. Hasegawa, Opt. Lett. 9 (1984) 288.
- [47] K. Tai, A. Hasegawa, A. Tomita, Phys. Rev. Lett. 56 (1986) 135.
- [48] S. Trillo, S. Wabnitz, Opt. Lett. 16 (1991) 986.
- [49] S. Coen, M. Haelterman, Phys. Rev. Lett. 79 (1997) 4139.
- [50] M. Peccianti, C. Conti, G. Assanto, A. De Luca, C. Umeton, Nature 432 (2004) 733.
- [51] Y.V. Kartashov, D.V. Skryabin, Optica 3 (2016) 1228.
- [52] E. Kengne, W.M. Liu, L.Q. English, B.A. Malomed, Phys. Rep. 982 (2022) 1.
- [53] T. Hansson, D. Modotto, S. Wabnitz, Phys. Rev. A 88 (2013) 023819.
- [54] Y.S. Kivshar, M. Peyrard, Phys. Rev. A 46 (1992) 3198.
- [55] B. Deconinck, K. Oliveras, J. Fluid Mech. 675 (2011) 141.[56] R.P. Creedon, B. Deconinck, O. Trichtchenko, J. Fluid Mech. 937 (2022) A24.
- [57] V.M. Hur, Z. Yang, Unstable stokes waves, 2022, arXiv:2010.10766.
- [58] B. Deconinck, S.A. Dyachenko, P.M. Lushnikov, A. Semenova, 2022. arXiv: 2211.05473.
- [59] K.B. Dysthe, K. Trulsen, Phys. Scr. T 82 (1999) 48.
- [60] A.I. Dyachenko, V.E. Zakharov, JETP Lett. 81 (2005) 255.
- [61] J.M. Dudley, F. Dias, M. Erkintalo, G. Genty, Nat. Photonics 8 (2014) 755.
- [62] M. Onorato, S. Residori, U. Bortolozzo, A. Montina, F.T. Arecchi, Phys. Rep. 528 (2013) 47.
- [63] F. Baronio, M. Conforti, A. Degasperis, S. Lombardo, M. Onorato, S. Wabnitz, Phys. Rev. Lett. 113 (2014) 034101.

- [64] B. Deconinck, J.N. Kutz, J. Comput. Phys. 219 (2006) 296.
- [65] N. Bottman, B. Deconinck, M. Nivala, J. Phys. A 44 (2011) 285201.
- [66] D.J. Frantzeskakis, J. Phys. A 43 (2010) 213001.
- [67] A. Weller, J.P. Ronzheimer, C. Gross, J. Esteve, M.K. Oberthaler, D.J. Frantzeskakis, G. Theocharis, P.G. Kevrekidis, Phys. Rev. Lett. 101 (2008) 130401.
- [68] S. Stellmer, C. Becker, P. Soltan-Panahi, E.M. Richter, S. Dörscher, M. Baumert, J. Kronjäger, K. Bongs, K. Sengstock, Phys. Rev. Lett. 101 (2008) 120406.
- [69] G. Theocharis, A. Weller, J.P. Ronzheimer, C. Gross, M.K. Oberthaler, P.G. Kevrekidis, D.J. Frantzeskakis, Phys. Rev. A 81 (2010) 063604.
- [70] P.G. Kevrekidis, D.J. Frantzeskakis, R. Carretero-González, The Defocusing Nonlinear SchrÖdinger Equation: From Dark Solitons to Vortices and Vortex Rings, SIAM, Philadelphia, 2015.
- [71] Y. Kawaguchi, M. Ueda, Phys. Rep. 520 (2012) 253.
- [72] D.M. Stamper-Kurn, M. Ueda, Rev. Modern Phys. 85 (2013) 1191.
- [73] T. Lahaye, C. Menotti, L. Santos, M. Lewenstein, T. Pfau, Rep. Progr. Phys. 72 (2009) 126401.